DOI: 10.15480/882.9362

Eighth International Symposium on Marine Propulsors
smp'24, Berlin, Germany, March 2024

Numerical noise prediction in multi-phase flows, a mesh sensitivity study*

Adrian Portillo-Juan[1], Simone Saettone[2], Esteban Ferrer[3,4]

[1]CEHINAV - Canal de Ensayos Hidrodinámicos de la ETSI Navales, Universidad Politécnica de Madrid, Avenida de la Memoria 4, 28040, Madrid, Spain
[2]Bound4blue, C/ Marie Curie 2, nave 14 08210 Barberà del Vallès Barcelona Spain
[3]ETSIAE-UPM-School of Aeronautics, Universidad Politécnica de Madrid, Plaza Cardenal Cisneros 3, 28040 Madrid, Spain
[4]Center for Computational Simulation, Universidad Politécnica de Madrid, Campus de Montegancedo, Boadilla del Monte, 28660 Madrid, Spain

ABSTRACT

The paper reports a mesh sensitivity study of a NACA $66_2 - 415$ elliptic wing hydro-acoustic simulations. The numerical calculations were performed using a DDES approach with a $k - \omega$ SST turbulence model and a VOF Schnerr-Sauer Cavitation model. To compute the radiated noise, Ffowcs-Williams and Hawkings (FW-H) acoustic analogy was used, employing a Farassat 1A formulation and computing the quadrupole noise term. The results show good convergence for lift, drag and the linear terms of radiated noise, while the quadrupole volume term presents a slower convergence. Overall, the results compare well with the experiments.

Keywords

Ffowcs-Williams and Hawkings, Mesh Sensitivity, DDES Simulation, 3D-Foil, Noise Prediction.

1 INTRODUCTION

As reported by Frisk (2012), noise has increased vastly over the last decades, with a 3.3 dB/decade growth rate, following the same evolution with time as worldwide GDP and shipping. Because of the negative impact of Underwater Radiated Noise (URN) growth on marine life, there is an increasing awareness among the international authorities on the need of mitigating shipping acoustic emissions. Last IMO guidelines (IMO, 2014), shows this awareness and encourages to address shipping URN problem during the design stage of vessels. Considering these recommendations, the main noise emitter in a vessel is the propeller (American Bureau of Shipping, 2021). Nonetheless, propeller design has traditionally been directed towards optimizing the energy efficiency, without including their acoustic footprint as a design constraint, except for some specific areas like naval vessels (Hammer, N.O. & McGinn, R.F. 1978 and Boswell, R.J. & Cox, G.G. 1974), and for some concepts like Kappel (Andersen, P. & Schwanecke 1992, Andersen, P. 2000, Andersen, P. et al. 2004 and Andersen, P. et al. 2005) or CLT propellers (Perez Gomez, G. 1976 and Perez Gomez, G., Gonzalez-Adaliz, J. 1992, Gaggero et al. 2015 and Gaggero et al. 2016) . Thus, it is imperative to develop new methods which can help to perform a multi-objective design of propellers.

CFD has represented during the last decades a convenient solution for propeller design in terms of the time and money resources needed. Nonetheless, including noise prediction in this type of simulations is quite recent (Posa, A. et al. 2022a, 2022b, 2022c and 2022d). The aim of this paper is to construct a numerical set-up to analyze the hydro-acoustics of multi-phase flows (e.g. cavitating flows) with special attention to numerical convergence. The geometry selected is a NACA $66_2 - 415$ elliptic wing which was experimentally tested at TU-Delft Cavitation Tunnel, by Pennings (2015). The geometry used for the paper was originally tested for different operational conditions. This study is limited to $Re = 8.9 \times 10^5$ and $\sigma = 1.07$ for the flow conditions at 5° angle of attack

2 GEOMETRY

The geometry used is a half elliptic wing model with a NACA $66_2 - 415$ section. The model has an aspect ratio of 3 with a half-span of $0.150m$. The root chord has a $c_o = 0.1256m$ value and the minimum wing thickness was $0.3mm$ due to manufacturing restrictions. The wing was modelled in Rhinoceros as a closed surface (Figure 1).

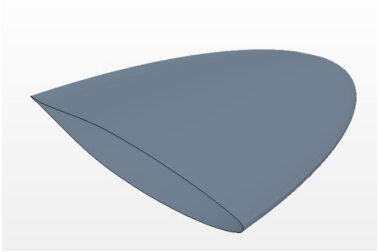

Figure 1: NACA $66_2 - 415$ Elliptic Wing

3 NUMERICAL METHOD

The simulations of the present work have been performed with the commercial solver SimCenter Star-CCM+ (2020). As the reference conditions come from a cavitating flow, the simulations will analyze highly unsteady situations, a Delayed Detached Eddy Simulation (DDES) approach will be used. The flow was modeled as a VOF-Multiphase model, with two different phases, water and vapour. Both fluids were defined with User Defined Equation of State as compressible fluids, which are needed to consider the non-linear terms of noise.

3.1 Domain definition

The simulation domain was defined as a squared section box of 2.13 x 0.3 x 0.3 m dimensions, which were the same as the test section of the experimental facility used to test the elliptic wing. Also, two different regions should be defined in hydro-acoustics simulations. The fluid domain region, which correspond to the whole domain, and where the pressure and velocity field was resolved and the acoustic region. This region, is the one in which the noise sources are directly computed. Consequently, this region will need a finer mesh, and it will be smaller and confined in the fluid domain region. For the present study, the acoustic domain was defined as a small refined region that encapsulates the elliptic wing and its boundary layer to capture all the pressure fluctuations originating from the foil, without increasing the computational cost.

The base cell size used corresponded to $1/5$ the chord length ($30mm$), and two refinements were performed, in the wing wall and the acoustic region. For the boundary layer modeling, as simulations are model-scaled, wall functions should not be implemented, thus a Low Y+ Wall Treatment should be used. However, this implies using Y+ values of 1, which is too computationally expensive. Thus an All Y+ Wall Treatment is used. The boundary layer is modeled based on the wall thickness, which is calculated based on the shear stresses (see equation 1).

$$\tau = \frac{\mu \cdot |v_{tang}|}{y} \tag{1}$$

Where v_{tang} is the tangential velocity vector, y is the wall distance and μ represents the dynamic viscosity. The velocity wall function can be defined based on the shear stresses as shown in equation 2. In this case, a blended wall function is used.

$$u^* = \gamma \sqrt{\frac{\mu \, |v_{tangential}|}{\rho y}} + (1-\gamma) C_\mu^{1/4} k^{1/2} \tag{2}$$

Where C_μ is a model coefficient, κ is the turbulent kinetic energy and γ is the blending function, which is obtained by equation 3

$$\gamma = 10^{-Re_d/11} \tag{3}$$

Where Re_d is the wall thickness Reynolds number. Thus, the wall thickness values can be obtained with equations 4 and 5.

$$y_{min} = \frac{u^+ \cdot y_1^+}{\rho} \tag{4}$$

$$y_{total} = \frac{u^+ \cdot y_{total}^+}{\rho} \tag{5}$$

Where y_1^+ and y_{total}^+ are the Y+ value for the first prism layer, and the total boundary layer respectively, which are set as 20 and 300, and $u+$ can be computed as shown in 6.

$$u^+ = \frac{u}{u^*} \tag{6}$$

An overview of the final mesh definition is shown in Figure 2.

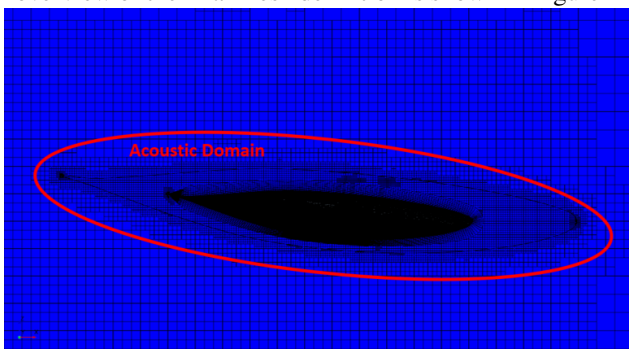

Figure 2: Mesh Definition

Using this domain definition, a Mesh Sensitivity study was perform, employing the ITTC (2021) Recommendations. Hence, six different cell sizes were used (Table 1), with a mesh refinement ratio between each mesh of $\sqrt{2}$.

Table 1: Mesh Definition

ID	Mesh	Cell Size (mm)	Nº Cells	
M1	Very Fine	21.21	2,4 mill	
M2	Fine	30.00	1,7 mill	
M3	Medium	42.43	800000	
M4	Medium-Coarse	60.00	400000	
M5	Coarse	84.85	260000	
M6	Very Coarse	120.00	150000	

3.2 Boundary Conditions

After defining the simulation domain and the main mesh parameters, the boundary conditions definition is needed. For the present simulations, the boundary conditions are defined as displayed in Figure 3.

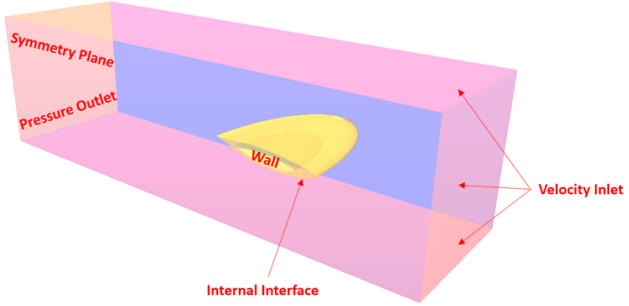

Figure 3: Boundary Conditions

3.3 Cavitation Model

For the present work, a VOF Multiphase approach is used, thus, the volume fraction of vapor is defined as shown in

(7).

$$\alpha_v = \frac{V_v}{V} = \frac{V_v}{V_v + V_l} \tag{7}$$

Where V_v is the volume fraction of vapor and V_l is the volume fraction of the liquid phase. The relationship between both phases is defined by (8).

$$V_v = n_0 \cdot V_l \cdot \frac{4}{3}\pi \cdot R_0^3 \tag{8}$$

Where n_0 is the nuclei population and R_0 is the considered bubble radius. Cavitation is modeled as a phase interaction with a Schnerr-Sauer model. This model neglects the effect of bubble growth acceleration, surface tension and viscous effects. Thus, bubble growth is estimated through an inertia controlled growth model (Equation 9).

$$v_r^2 = \frac{2}{3}\left(\frac{p_{sat} - p}{\rho_l}\right) \tag{9}$$

3.4 URN

To predict the noise production of the test-case wing, the FW-H acoustic analogy (Ffowcs-Williams, J. & Hawkings, D.L. (1969)) was used. This analogy uses the pressure field computed for a certain region and/or surfaces from the simulation domain. In contrast with aero-acoustics problems, for hydro-acoustics, non-linear quadrupole noise originating from cavitation can become significant. Hence, to properly account cavitating noise, a porous formulation needs to be implemented (Bensow, R. & Liefvendahl, M. 2016, Kimmerl, J. & Abdel-Maksoud, M. 2023 and Dlamini, K.M. et al. 2023). For the test case used, this was addressed through a permeable surface defined by the acoustic region interface and an impermeable surface for the wing wall boundary. The acoustic analogy uses the flow field solution as an input and rearranges the continuity and momentum equation into an inhomogeneous wave equation. The radiated pressure obtained is divided in three terms, loading, thickness and quadrupole volume terms.

$$p'(\mathbf{x},t) = p'_L(\mathbf{x},t) + p'_T(\mathbf{x},t)` + p'_Q(\mathbf{x},t) \tag{10}$$

Where p'_T and p'_L form the total surface term, which is the linear component while p'_Q represents the non-linear term. These terms are calculated as displayed at equations 11 to 13.

$$p_T\prime(\mathbf{x},t) = \frac{1}{4\pi}\left(\left(\frac{\partial}{\partial t}\right)\int_S \left[\frac{Q}{r(1-M_r)}\right]_{ret} dS\right) \tag{11}$$

$$p_L\prime(\mathbf{x},t) = \frac{1}{4\pi}\left(\left(-\frac{\partial}{\partial x_i}\right)\int_S \left[\frac{L_i}{r(1-M_r)}\right]_{ret} dS\right) \tag{12}$$

$$p_Q\prime(\mathbf{x},t) = \frac{1}{4\pi}\left(\left(\frac{\partial^2}{\partial x_i \partial x_j}\right)\int_V \left[\frac{T_{ij}}{r(1-M_r)}\right]_{ret} dV\right) \tag{13}$$

Where r is the distance from the FW-H surface to the computed point receiver, M_r represents the Mach number of the source, T_{ij} and L_j are the Lighthill stress tensor and compressive stresses tensor respectively and Q is defined by (14).

$$Q = \rho_0 U_i n_i \tag{14}$$

Where U_i is the flow velocity field and n_i is the surface normal vector. As it can be observed, the linear terms are integrated through a surface while the non-linear quadrupole term are computed through a volume. The former corresponds to the permeable surface boundary, while the second one corresponds to the volume confined by the acoustic region. The formulation used for the present study is Farassat 1A Formulation (Farassat, F. (1975)), which is the one preferred for general (non-rotating) subsonic regions.

After the FW-H noise sources are computed in the defined FW-H surface, a wave equation is used to propagate their contribution towards the observer (receiver) position. For the present paper, the point receiver was set in the same position as in the original experiments (Pennings, 2015).

3.5 Least Square Root Approach

For the mesh sensitivity study, for the present research work, the least square root approach (based on the Richardson extrapolation method) has been implemented, which is the one recommended by the ITTC (2021). This method requires to use a minimum of four grids, from which a curve fit (15) will be built.

$$S_i = S_0 + \alpha h_i^p \tag{15}$$

Where S_i is the solution of the $i^t h$ mesh, S_0 the extrapolated result to zero step, h_i is the step size, p is the order of accuracy and α represents a constant. Based on the above equation, the discretization error can be derived. (Equation 16).

$$\epsilon_{RE} \approx \delta_{RE} = S_i - S_0 = \alpha * h_i^p \tag{16}$$

Where α, p and S_0 are unknown variables. These values can be estimated by minimizing the mean squared root deviation of the scatter observed in the group of solutions (17).

$$f(p,\alpha,S_0) = \sqrt{\sum_{i=1}^{n_m}(S_i - (S_0 + \alpha h_i^p))^2} \tag{17}$$

Where n_g corresponds to the number of mesh conditions. Based on the obtained p value, the numerical uncertainty can be computed (18).

$$\begin{cases} 0.95 \leq p \leq 2.05 : U_{SN} = 1.25\delta_{RE} + U_{SD} \\ p < 0.95 : U_{SN} = min(1.25\delta_{RE} + U_{SD}, 3\delta_{RE}^{12} + U_{SD}^{12}) \\ p > 2.05 : U_{SN} = max(1.25\delta_{RE} + U_{SD}, 3\delta_{RE}^{02} + U_{SD}^{02}) \end{cases} \tag{18}$$

Where U_{SD}^{ij} correspond to the standard deviation of the curve fit built with δ_{RE}^{ij}. These values are computed as shown in equations 19 to 24.

$$U_{SD} = \sqrt{\frac{\sum_{i=1}^{n_m}(S_i - (S_0 + \alpha h_i^p))^2}{n_m - 3}} \tag{19}$$

$$U_{SD}^{02} = \sqrt{\frac{\sum_{i=1}^{n_m}(S_i - (S_0 + \alpha_{02} h_i^2))^2}{n_m - 3}} \tag{20}$$

$$U_{SD}^{12} = \sqrt{\frac{\sum_{i=1}^{n_m}(S_i - (S_0 + \alpha_{11}h_i + \alpha_{12}h_i^2))^2}{n_m - 3}} \quad (21)$$

$$\delta_{RE} = \alpha h_i^p \quad (22)$$

$$\delta_{RE}^{02} = \alpha_{02} h_i^2 \quad (23)$$

$$\delta_{RE}^{12} = \alpha_{11} h_i + \alpha_{12} h_i^2 \quad (24)$$

4 RESULTS

In the following sections the computed results for the flow and acoustic field are displayed. The conditions used for the simulations are the same as described in previous sections.

4.1 Flow results

The first results to be analyzed correspond to the lift and drag coefficients. The results obtained for both coefficients for the different grids studied are displayed at Figures 4 and 5.

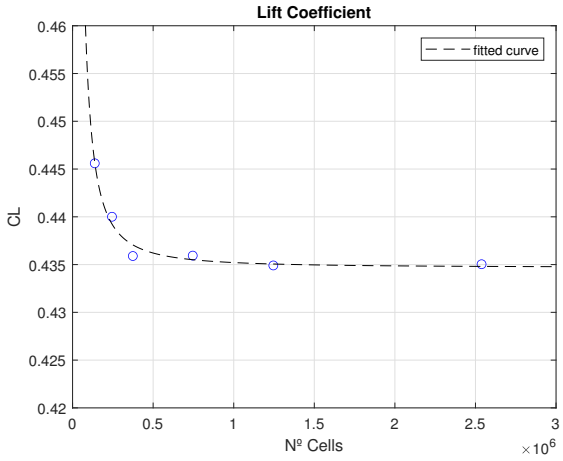

Figure 4: Lift Coefficient Mesh Sensitivity Study

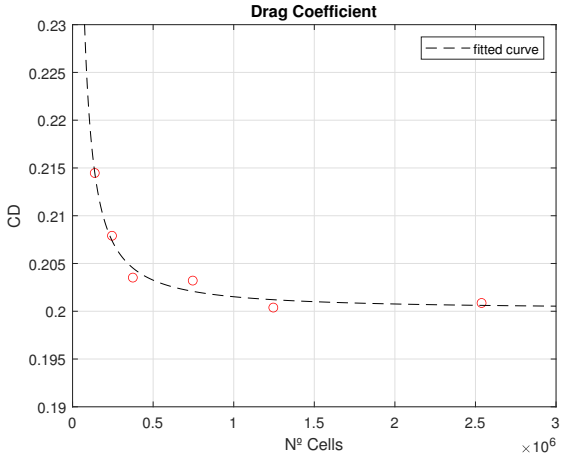

Figure 5: Drag Coefficient Mesh Sensitivity Study

The figures present the verification process done for the lift and drag coefficients. From the computed results it can be observed that both drag and lift present good convergence, with a quadratic evolution towards mesh resolution. As explained above, the verification process was done following the 1least square root approach. The numerical uncertainties and p values obtained are displayed at Table 2.

Table 2: Lift and Drag coefficient verification results

C_L			C_D		
Mesh	p	UN	Mesh	p	UN
M2	2.41	0.41	M2	1.81	0.81
M1	2.41	0.66	M1	1.81	1.15
M3	2.41	1.14	M3	1.81	1.76
M4	2.41	2.11	M4	1.81	2.94
M5	2.41	4.01	M5	1.81	5.05
M6	2.41	7.75	M6	1.81	8.83

From the flow results evolution with mesh refinement it can be observed that both drag and lift present an appreciable sensitivity to mesh refinement. This is shown in a quadratic evolution with the grid size which leads to an asymptotic range of results in both cases. When the numerical uncertainties (UN) and p values were estimated some observations could be stated. First, the p value was around 2 for both lift and drag, which is the theoretical value that p should take for Navier Stokes equations problems. This is as well coherent with the quadratic evolution appreciated in figures 4 and 5. In terms of the numerical uncertainty it should be noted that in all cases it was below 10% with values under 2% of uncertainty for grids of uncertainty for grids with over 1 mill. cells.

To analyze the relation between grid resolution and simulation time cost, the uncertainties were compared towards the simulation time (6).

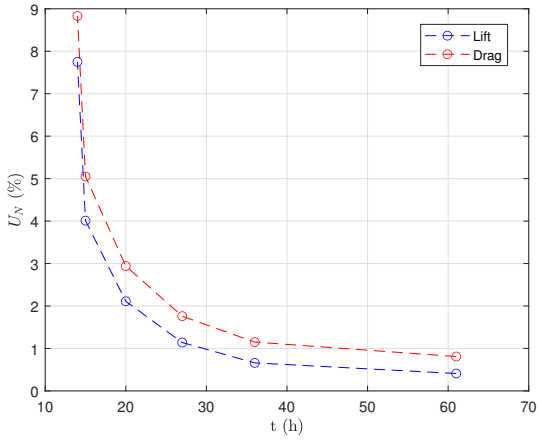

Figure 6: Uncertainties vs. time cost (drag and lift)

As can be expected, the uncertainties present a similar evolution towards time consumption as C_L and C_D with the mesh resolution. However, the asymptotic range in terms of time consumption is reached later. Considering all these aspects, the least expensive mesh which would present converged C_D, C_L and uncertainty values would be $M1$ which correspond to the fine mesh.

For the selected mesh, C_L showed a 5% deviation from the experimental results. Also, to analyze the capture of cavitation phenomena, pressure distribution, vorticity and vapor volume was evaluated. The results of these parameters are displayed in figures 7 to 9.

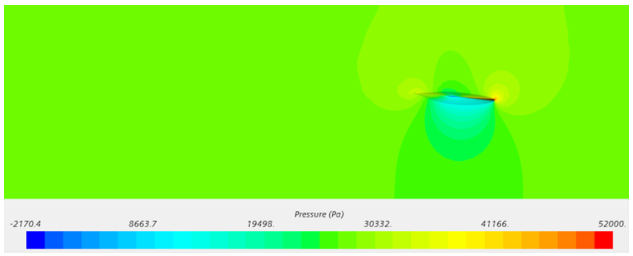

Figure 7: Pressure Field

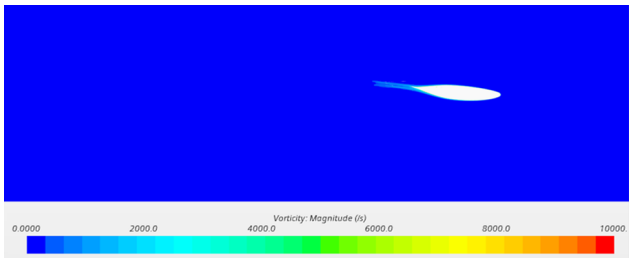

Figure 8: Vorticity

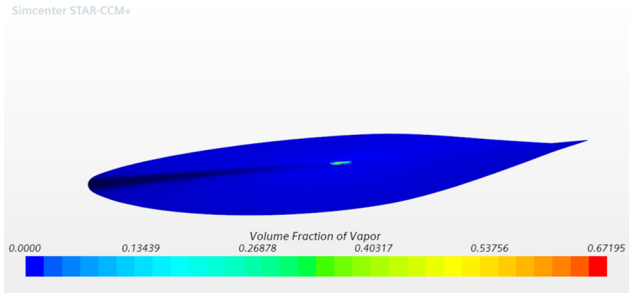

Figure 9: Volume fraction of vapor

The pressure field show a pressure drop originated in the tip of the wing which would lead to Tip Vortex Cavitation (TVC). This is later reflected in the volume fraction of vapor. However, TVC was not fully developed. This can be justified by the fact that TVC is the first form of cavitation, and thus, finer meshes would be needed to capture bubble creation, growth and collapse. Regarding vorticity, it can be observed that for this angle of attack, flow is overall well-behaved, and flow separation is negligible.

4.2 Acoustic results

Due to the highly unsteady behavior of sound, the verification process can become a challenging process. To address this task, the computed radiated pressure components from the FW-H at the point receiver location have been used. Consequently, the parameter used to address the sound verification corresponds to the summation of the signals radiated from each element of the FW-H surface at the point receiver during the simulation time. Nonetheless, these values fluctuate in time domain. In Figures 10 to 12 the evolution of $p_S\prime$, $p_Q\prime$ and $p\prime$ at 5° of attack from the impermeable case for the selected mesh is shown as an example. It must be noted that, the results from the permeable case showed remarkably higher fluctuations over time, and thus, a verification could not be performed. Nevertheless, the physics results showed valuable information regarding cavitating noise source localization.

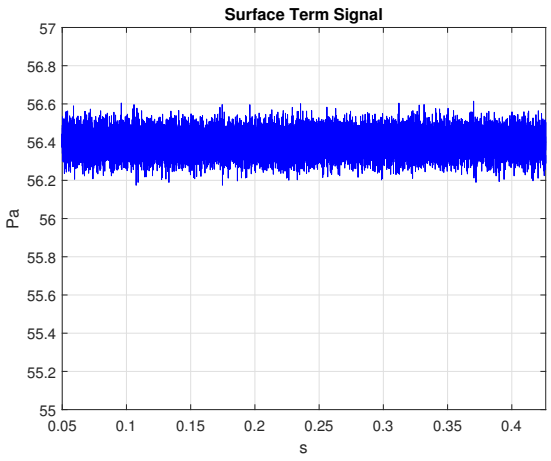

Figure 10: Surface Total Term Signal

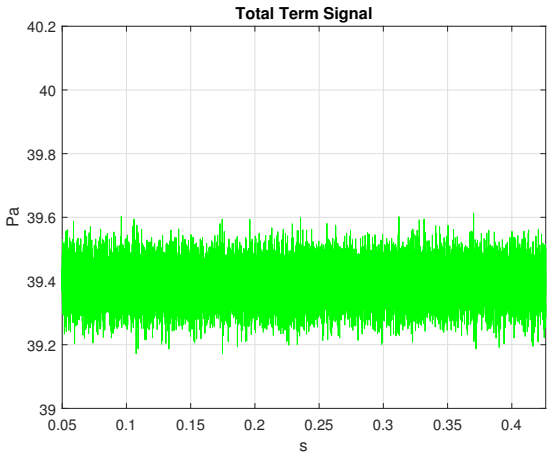

Figure 11: Quadrupole Volume Term Signal

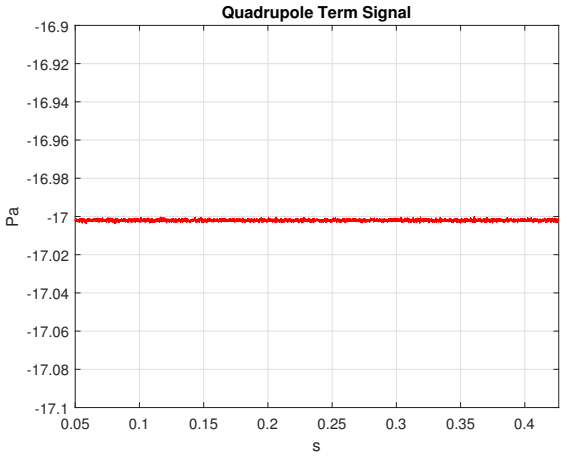

Figure 12: Total Term Signal

Firstly, it can be observed that the fluctuating part of noise corresponds to the surface term contribution. This is observed in a greater amplitude of the signal compared to the quadrupole signal amplitude (0.44 Pa vs. 3.06 mPa). This explains the resemblance between surface and total term signals and also suggests a minor contribution of the non-linear terms to the propagated noise. To address the

verification process and compute the numerical uncertainties, the mean value of the signals will be used.

First, the total surface term and quadrupole volume term mean values convergence was analyzed at the selected angle of attack (see Figures 13 and 14).

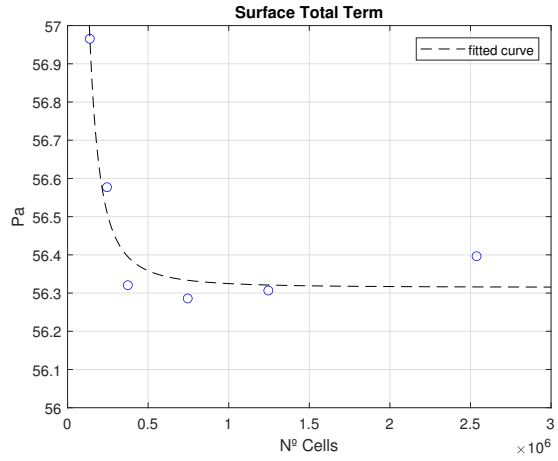

Figure 13: Total Surface Noise Term Verification (5º)

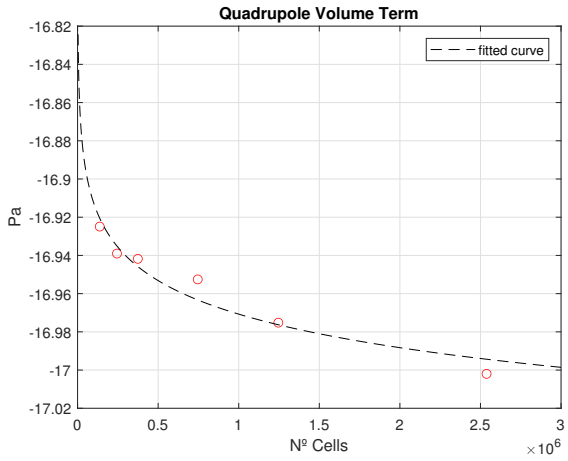

Figure 14: Quadrupole Volume Noise Term Verification (5º)

From figures 13 and 14, some appreciations can be done. Firstly, the surface term shows a clear convergence with a good and fast evolution towards an asymptotic range. Regarding the quadrupole term, although a certain convergence is observed, finer meshes would be needed to fully reach the asymptotic range in the results. The p values and the uncertainties obtained for the linear and quadrupole components are displayed in Table 3.

Table 3: Noise Terms Verification Results

$p_{S'}$			$p_{Q'}$		
Mesh	p	UN	Mesh	p	UN
M2	2.67	0.36	M2	0.83	0.18
M1	2.67	0.40	M1	0.83	0.23
M3	2.67	0.63	M3	0.83	0.30
M4	2.67	1.09	M4	0.83	0.39
M5	2.67	2.00	M5	0.83	0.51
M6	2.67	3.81	M6	0.83	0.72

As already observed, the surface term presents a p value over 2. This shows a quadratic behaviour with a fast convergence. The uncertainties obtained are low for all mesh conditions, lying under a 1% of deviation for those in the asymptotic range. Regarding the quadrupole terms, p value drops to values close to 1. This is in line with the behavior observed at Figure 14 and it indicates a linear behaviour. Nevertheless, the uncertainties obtained in this case were as well low, within a 0.5% for the medium, fine and very fine mesh conditions.

If the evolution of the quadrupole and surface terms values with the mesh definition are compared it can be observed that the linear term presents a higher sensitivity to mesh refinements. Thus, the total noise convergence was also analyzed (Figure 15).

From the evolution shown in Figure 15 it can be observed that the total noise term presents a fast convergence and the asymptotic range is fully reached for the medium, fine and very fine mesh conditions.

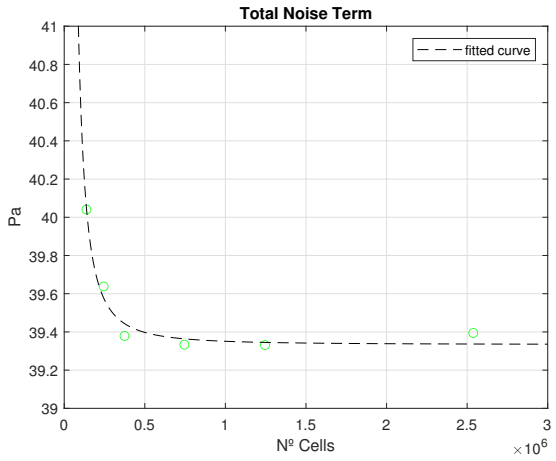

Figure 15: Total Volume Noise Term Verification (5º)

The p values and numerical uncertainties were also estimated (4). From these results similar appreciations as the one for the surface term can be done. Hence, although the non-linear term presents a slower convergence, this has a minor contribution to the overall convergence of acoustic pressure.

Table 4: Noise Terms Verification Results

$p_{T'}$		
Mesh	p	UN
M2	2.94	0.37
M1	2.94	0.55
M3	2.94	0.91
M4	2.94	1.62
M5	2.94	3.03
M6	2.94	5.80

After analyzing the convergence of the different FW-H noise terms, it is important to analyze as well the convergence of uncertainties with time, in view of selecting one mesh to compare with experimental results. This study is shown in figure 16

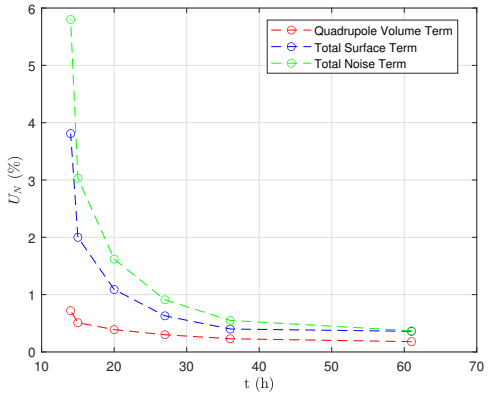

Figure 16: Numerical uncertainties vs. Simulation time

Considering this analysis and the prior ones, the mesh that best full-fills the requirements of converged results, low uncertainties and an affordable time cost would be the fine mesh (M1).

For the selected mesh, the noise terms and SPL spectrum were analyzed (figures 17 to 19). As introduced before, the noise terms distribution data was extracted from the permeable FW-H surface.

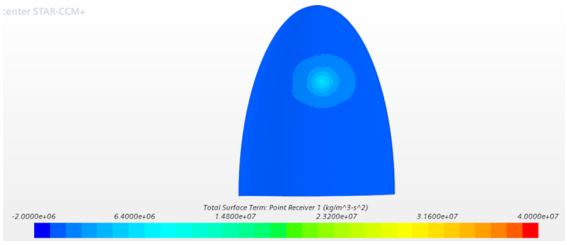

Figure 17: Surface total term. Suction side.

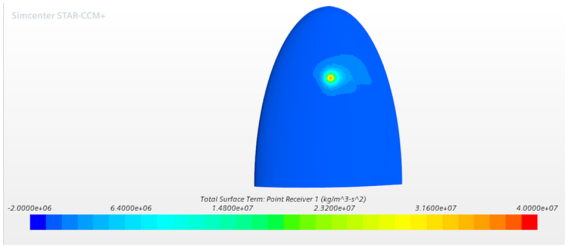

Figure 18: Surface total term. Pressure side.

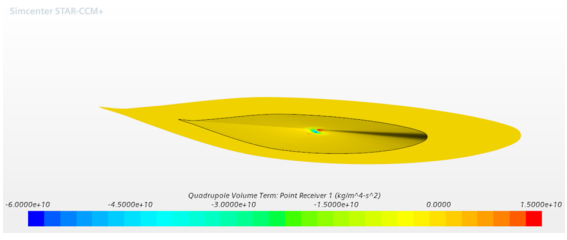

Figure 19: Quadrupole volume term.

From the surface term it can be observed that while the major contribution comes from the loading, monopole, term; the thickness term presents a minor effect to noise generation. Also, it can be appreciated that while the surface term is originated from the pressure and suction side of the wing, the quadrupole term originates in the tip. Nevertheless, it can be noticed that the monopole and quadrupole contributions mostly originate from the boundary layer region.

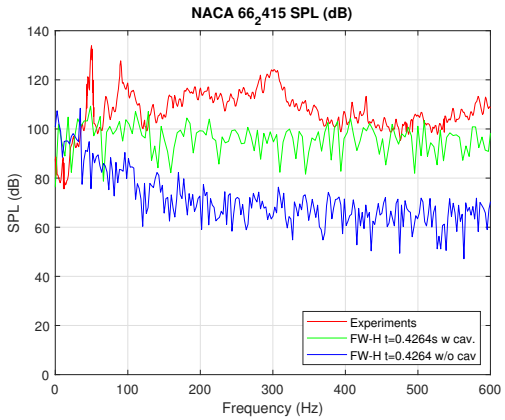

Figure 20: URN Prediction. CFD vs. Experimental results

When the SPL spectrum was compared with the experiments in both cavitating and non-cavitating conditions (20), some observations could be drawn. First, the effect of activating cavitation models can be stated. However, although the broadband noise was well captured, with deviations of less than 10dB, the tonal peaks which occured between 170-250 Hz were not captured. This can be justified by the underestimation of the generated vapor volume. The tonal peaks below 100 Hz found in the experimental results (Pennings, 2015) can be attached to the tunnel.

5 CONCLUSIONS

From the analysis shown above several conclusions can be outlined. A numerical prediction of the noise produced by a 3-D half-elliptic wing has been performed. The results show in first place that coupling acoustic analogies with CFD solvers has a minor impact on time resources and it does not affect hydrodynamic (lift and drag) predictions.

From the noise generation computed results, two main conclusions can be drawn. Firstly, using an impermeable FW-H surface approach proved to have better convergence results than a permeable FW-H approach with small numerical uncertainties. Secondly, fair agreement with the experiments was obtained, with a mean deviation of 10-15 dB in the low-medium frequency range. It should be noted that these deviations found depend to a great extent on the frequency. However, the main tonal peaks, caused by the cavitating conditions were not captured.

Lastly, some appreciations were as well extracted from the effect of cavitation on noise generation. Firstly, although TVC was generated in the numerical model, it was weakly captured, and TVC stream was not fully developed. This can be attached to the mesh refinement outside the acoustic region. Secondly, the importance of considering cavitation models in these types of numerical studies can be stated. It was appreciated that if cavitation phenomena are not properly modeled, deviations can increased up to 40 dB for frequencies above 100 Hz. Also, from this conclusion, the impact of cavitation on noise generation can be reinforced.

For the present test-case, cavitation can potentially increase SPL one order of magnitude.

6 ACKNOWLEDGEMENTS

Adrian Portillo-Juan has received funding from Universidad Politécnica de Madrid as a beneficiary of one of the Pre-doctoral contracts of the UPM research programe and from Fundación Centro Tecnológico SOERMAR. This research has also received funding from the European Union (ERC, Off-coustics, project number 101086075). Views and opinions expressed are however those of the author(s) only and do not necessarily reflect those of the European Union or the European Research Council. Neither the European Union nor the granting authority can be held responsible for them. Esteban Ferrer and Adrian Portillo would like to thank the support of Agencia Estatal de Investigación for the grant "Europa Excelencia" for the project EUR2022-134041 funded by MCIN/AEI/10.13039/501100011033) and the European Union NextGenerationEU/PRTR.

REFERENCES

Andersen & Schwanecke (1992). 'Design and model tests of tip fin propellers.'

Andersen (2000). 'Cavitation consideration in the design of kappel propellers.' Proc. of NCT'50, Int. Conference on Propeller Cavitation **1010**

Andersen, Friesch, & Kappel (2004).'Development and full-scale evaluation of a new marine propeller type.' Schiffbautechnische Gesellschaft 465-476.

Andersen, Friesch, Kappel, Lundergaard, & Graham (2005).'Development of a marine propeller with nonplanar lifting surfaces.' Marine technology and SNAME news **42(03)** 144-148.

Bensow, & Liefvendahl, (2016). 'An acoustic analogy and scale-resolving flow simulation methodology for the prediction of propeller radiated noise.' 31st Symposium on Naval Hydrodynamics, 11-16.

Boswell, & Cox, (1974) 'Design and evaluation of a highly skewed propeller for a cargo ship'. Technical report, Department of the Navy, Naval Ship Research and Development Center.

Farassat, (1975) 'Theory of noise generation from moving bodies with an application to helicopter rotors.' Technical report.

Frisk, (2012). 'Noiseonomics: The relationship between ambient noise levels in the sea and global economic trends.' Sci Rep. **2** (437)

Gaggero, Viviani, Gonzalez-Adalid, Perez Sobrino, Gennaro, Sanguinetti, & Bina (2015) 'A design by optimization of tip loaded propellers.', Fourth International Symposium on Marine Propulsors, Austin, Texas.

Gaggero, Gonzalez-Adalid, & Perez Sobrino, (2016) 'Design and analysis of a new generation of clt propellers.', Applied Ocean Research, **59**, 424-450.

Hammer, & McGinn, (1978). 'Highly skewed propellers - full scale vibration test results and economic considerations'. Technical report.

IMO. (2014). 'Guidelines for the reduction of underwater noise from commercial shipping to address adverse impacts on marine life.' MEPC.1/Circ.833 , London, United Kingdom.

Kimmerl, & Abdel-Maksoud, (2023) 'Visualization of underwater radiated noise in the near-and far-field of a propeller-hull configuration using CFD simulation results.' Journal of Marine Science and Engineering, **11(4)**.

Ffowcs-Williams, & Hawkings, (1969) 'Sound generation by turbulence and surfaces in arbitrary motion.' Philosophical Transactions of the Royal Society of London. Series A, Mathematical and Physical Sciences, **264(1151)**.

Perez Gomez, (1976). 'Una innovación en el proyecto de hélices.' Ingeniería Naval, Spain.

Perez Gomez, & Gonzalez-Adalid, (1992) 'Tip loaded propellers (CLT). justification of their advantages over high skewed propellers using the new momentum theory. SNAME New York Metropolitan Section, Fiftieth Anniversary.

Pennings, (2015). 'Dynamics of Tip Vortex Cavitation'. TU-Delft University, Delft, Netherlands.

Pennings, Bosschers, Westerweel & van Terwisga (2014). ' Dynamics of isolated vortex cavitation'. Journal of Fluid Mechanics, **778** 288-313

Dlamini, K.M., Hashe, V.T. & Kunene, T.J. (2023) 'Numerical modeling of cavitation rates and noise acoustics of marine propellers.' Mathematical and Computational Applications, **28(2)**

American Bureau of Shipping, (2021). 'Practical considerations for underwater noise control', ABS, White paper.

Posa, A., Felli, M., & Broglia, R. (2022) 'The signature of a propeller- rudder system: Acoustic analogy based on LES data.' Ocean Engineering, **259**.

Posa, A., Felli, M., & Broglia, R. (2022) 'Influence of an upstream hydrofoil on the acoustic signature of a propeller'. Physics of Fluids, **34(4)**.

Posa, A., Broglia, R., Felli, M., Cianferra, M. & Armenio, V. (2022) 'Hydroacoustic analysis of a marine propeller using large-eddy simulation and acoustic analogy.', Journal of Fluid Mechanics, **947:A46**.

Posa, A., Broglia, R. & Felli, M. (2022) 'Acoustic signature of a propeller operating upstream of a hydrofoil.', Physics of Fluids, **34(6)**.

SimCenter Star-CCM+ (2020). Star-CCM+ v15.04.008 Tutorial guide.

ITTC (2021), 'Uncertainty Analysis in CFD Verification and Validation, Methodology and Procedures', ITTC Recommended Procedures and Guidelines **7.5-03-01-01**